Phase Conversion from Hexagonal CuSySe₁₋ᵧ to Cubic Cu₂₋ₓSySe₁₋ᵧ: Composition Variation, Morphology Evolution, Optical Tuning, and Solar Cell Applications

Jun Xu,*[†,‡] Xia Yang,[‡] Qingdan Yang,[‡] Wenjun Zhang,[‡,§] and Chun-Sing Lee*[‡,§]

[†]School of Electronic Science and Applied Physics, Hefei University of Technology, Hefei, 230009, People's Republic of China
[‡]Center of Super-Diamond and Advanced Films, Department of Physics and Materials Science, City University of Hong Kong, Hong Kong SAR, People's Republic of China
[§]City University of Hong Kong Shenzhen Research Institute, Shenzhen, 518057, People's Republic of China

Ⓢ Supporting Information

ABSTRACT: In this work, we report a simple and low-temperature approach for the controllable synthesis of ternary Cu−S−Se alloys featuring tunable crystal structures, compositions, morphologies, and optical properties. Hexagonal CuSySe₁₋ᵧ nanoplates and face centered cubic (fcc) Cu₂₋ₓSySe₁₋ᵧ single-crystal-like stacked nanoplate assemblies are synthesized, and their phase conversion mechanism is well investigated. It is found that both copper content and chalcogen composition (S/Se atomic ratio) of the Cu−S−Se alloys are tunable during the phase conversion process. Formation of the unique single-crystal-like stacked nanoplate assemblies is resulted from oriented stacking coupled with the Ostwald ripening effect. Remarkably, optical tuning for continuous red shifts of both the band-gap absorption and the near-infrared localized surface plasmon resonance are achieved. Furthermore, the novel Cu−S−Se alloys are utilized for the first time as highly efficient counter electrodes (CEs) in quantum dot sensitized solar cells (QDSSCs), showing outstanding electrocatalytic activity for polysulfide electrolyte regeneration and yielding a 135% enhancement in power conversion efficiency (PCE) as compared to the noble metal Pt counter electrode.

KEYWORDS: CuSySe₁₋ᵧ, Cu₂₋ₓSySe₁₋ᵧ, composition tuning, optical properties, counter electrodes
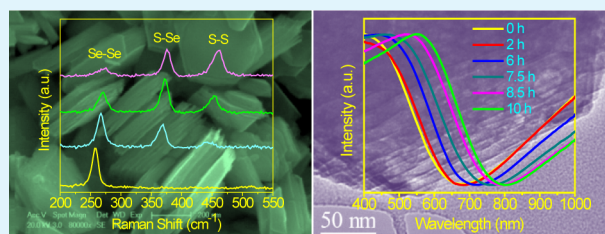
■ INTRODUCTION

Composition engineering, including doping and stoichiometry variation, enables custom tuning of chemical and physical properties of semiconductors. Ternary alloyed semiconductors not only add another dimension of composition engineering over their binary counterparts, they often inherit merits from their parent binary materials and show additional new properties.[1−6] Copper chalcogenides (Cu₂₋ₓS, Cu₂₋ₓSe) are promising candidates as sustainable energy materials, due to their low toxicity, earth abundance, and suitable band gaps, and tunable ratio of copper and chalcogen.[7−9] They have been widely applied in solar cells, near-infrared (NIR) photothermal therapy, lithium ion batteries, gas sensors, and electronic and optoelectronic devices.[10−14]

Ternary Cu−S−Se alloyed semiconductors are attracting increasing attention as they are considered to possess not only the merits and advantages of binary copper chalcogenides (Cu₂₋ₓS, Cu₂₋ₓSe) but also unique properties from the chalcogen composition variation. It is documented that copper vacancy tuning in binary copper chalcogenides (Cu₂₋ₓS, Cu₂₋ₓSe) is a powerful method to adjust their NIR absorption that originated from localized surface plasmonic resonance (LSPR) of free holes in the valence band.[15−19] Both Cu₂₋ₓS and Cu₂₋ₓSe show enhanced NIR absorption with increasing

copper vacancies.[15−19] On the other hand, S/Se atomic ratio tuning can well control the band-gap absorption and emission properties of multinary copper chalcogenides.[20,21] For Cu−S−Se alloys, there will be two independent approaches, i.e., cation vacancy tuning and anion composition variation, to modulate their physical and chemical properties. Therefore, it is of great significance for controllably synthesizing Cu−S−Se alloys and understanding the influence of composition variation on material properties and device performance.

To date, there are only a few reports on alloyed Cu−S−Se nanostructures (including Cu₂₋ₓSySe₁₋ᵧ and Cu₂SySe₁₋ᵧ), which were typically prepared at high temperature (>200 °C) using solvothermal methods.[22−27] Copper content tuning and phase conversion among the ternary Cu−S−Se alloys have never been investigated. Energy conversion applications of the Cu−S−Se alloys are seldom explored. In this work, we report a simple and facile approach to synthesize hexagonal CuSySe₁₋ᵧ nanoplates and face centered cubic (fcc) Cu₂₋ₓSySe₁₋ᵧ single-crystal-like stacked nanoplate assemblies at a low temperature of 100 °C. Composition variation and morphology evolution

during the phase conversion from hexagonal CuS_ySe_{1-y} to fcc $Cu_{2-x}S_ySe_{1-y}$ are investigated. Optical properties of the Cu–S–Se alloys are systematically tuned through composition variation, including both copper content and S/Se atomic ratio variations. Furthermore, to demonstrate potential utilities of the novel Cu–S–Se alloys in energy conversion devices, the alloys are employed for the first time as efficient CEs with improved electrocatalytic activity to replace the noble Pt electrode for catalyzing polysulfide electrolyte regeneration in quantum dot sensitized solar cells (QDSSCs).

EXPERIMENTAL SECTION

Synthesis of CuS_ySe_{1-y} Nanoplates and $Cu_{2-x}S_ySe_{1-y}$ Stacked Nanoplate Assemblies. In a typical synthesis, 0.75 mmol of S powder and 1.25 mmol of Se powder were dissolved in a 20 mL NaOH (5.0 M) aqueous solution in a beaker by heating and magnetic stirring. CuS_ySe_{1-y} nanoplates were obtained immediately upon adding 4 mL of $Cu(NO_3)_2$ ethanol solution (0.2 M) into the above solution (80–95 °C). Further heating the beaker in an oven at 100 °C for 10 h would lead to the formation of $Cu_{2-x}S_ySe_{1-y}$ stacked nanoplates. The samples were collected and washed sequentially with hot distilled water, diluted HCl solution, and ethanol several times, and then vacuum-dried. For tuning the ratio of S/Se in the nanoplates, the above processes were repeated by using different relative amounts of S and Se powders (0:2, 0.5:1.5, 0.75:1.25, and 1:1 in molar ratios) in the reactants.

Preparation of Counter Electrodes. Counter electrodes were prepared by spin-coating the as-prepared CuS_ySe_{1-y} nanoplates and the $Cu_{2-x}S_ySe_{1-y}$ stacked nanoplate assemblies onto fluorine doped tin oxide (FTO) glass substrates followed by annealing at 350 °C in nitrogen. For comparison, a conventional platinized FTO (Pt/FTO) counter electrode was also prepared.

Preparation of Photoanodes. For photovoltaic applications, arrays of ZnO/ZnSe/CdSe/ZnSe nanocables were used as photoanodes, which were prepared by a modified ion exchange method.[28,29] Arrays of ZnO nanowires with lengths of about 12 μm grown on FTO glass substrates were prepared by a seed assistant hydrothermal growth method. Arrays of ZnO/ZnSe core/shell nanocables were prepared by immersing the ZnO nanowire arrays in a Se^{2-} ion solution (6.0 mM) prepared by reacting Se powder with $NaBH_4$, and kept at 50 °C for 2.5 h. This process was repeated two times to get a desirable thickness of ZnSe. The arrays of ZnO/ZnSe nanocables then reacted with a $Cd(NO_3)_2$ aqueous solution (25.0 mM) at 95 °C for 5 h to partially replace Zn^{2+} by Cd^{2+} in the ZnSe shell, resulting in formation of ZnO/ZnSe/CdSe nanocables. The ZnO/ZnSe/CdSe nanocable arrays were coated with ZnSe by twice dipping alternately into $Zn(NO_3)_2$ (25 mM) and Se^{2-} ion (6.0 mM) solutions for 30 min per dip, rinsing with deionized water between dips.

Fabrication of Solar Cells. Solar cells were prepared by assembling and bonding the photoanodes with different counter electrodes. The two electrodes were separated by a 60 μm thick polypropylene spacer, and the internal space of the cells was filled with a polysulfide electrolyte (1.0 M S, 1.0 M Na_2S, and 0.1 M NaOH in deionized water). The active area of the solar cells was 0.25 cm². During the course of the experiments, it was found that performance of the solar cells is sensitive to the morphologies, density, and length of the ZnO/ZnSe/CdSe/ZnSe nanocables. Thus, to exclude the influence from the photoanode, we used the same anode sample to make the different cells to achieve a fair comparison of the various counter electrodes.

Characterization. The as-prepared samples were characterized with X-ray diffraction (XRD) with a Philips X'Pert diffractometer using Cu Kα radiation. Scanning electron microscopy (SEM) and transmission electron microscopy (TEM) were carried out respectively with a Philips XL30 FEG SEM and a Philips CM 20 FEG TEM (or a Philips CM 200 FEG TEM or a JEOL JEM-2100F TEM, all operated at 200 kV). Electron energy loss spectroscopy (EELS) data were acquired with a Gatan Tridiem imaging filter attached to the JEOL

TEM. X-ray photoelectron spectroscopy (XPS) was performed in a VG ESCALAB 220i-XL UHV surface analysis system with a monochromatic Al Kα X-ray source (1486.6 eV). Raman measurements were conducted with a Renishaw 2000 laser Raman microscope equipped with a 514 nm argon ion laser for excitation. Optical absorption measurements were carried out by dispersing samples in absolute ethanol (0.2 mmol L^{-1}) via ultrasonication and measuring with a Shimadzu UV-3600 spectrophotometer. Current density–voltage (J–V) characteristics of the solar cells were measured under AM 1.5G illumination with an intensity of 100 mW cm^{-2}. Intensity of the solar simulator was calibrated by a standard silicon diode with a KG-5 filter to minimize error due to spectral mismatch. Electrochemical impedance spectroscopy (EIS) measurements were performed in the dark using an impedance measurement unit (ZAHNER-elektrik IM6) over the frequency range 0.1–10^5 Hz with an ac amplitude of 10 mV.

RESULTS AND DISCUSSION

Figure 1a shows an XRD pattern of the immediate product prepared by reacting Cu^{2+} ions with an alkaline sulfur/selenium
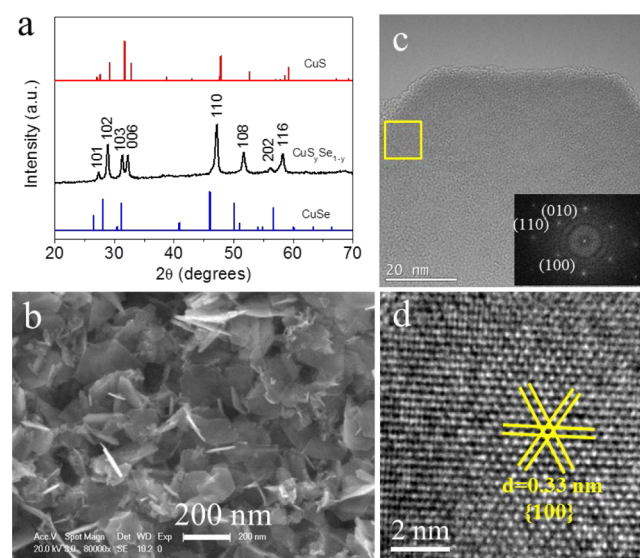

Figure 1. (a) XRD pattern, (b) SEM image, (c) HRTEM image and corresponding FFT (inset), and (d) enlarged HRTEM image of CuS_ySe_{1-y} ($y = 0.54$) nanoplates prepared with 0.75 mmol of S and 1.25 mmol of Se in the reactants.

(0.75 mmol/1.25 mmol) aqueous solution. Positions of the diffraction peaks are between those of the binary hexagonal CuSe (JCPDF 20-1020) and the hexagonal CuS (JCPDF 06-0464), and the overall diffraction pattern has a profile similar to those of the binary compounds. This confirms that the product is not a physical mixture of the two binary compounds and suggests the formation of a hexagonal phase alloy. The shifts in the diffraction peaks are attributed to changes in lattice parameters due to the coexistence of S and Se atoms. Figure 1b is a typical SEM image of the as-prepared hexagonal alloy, showing crystallites of plate shape with sizes of 100–200 nm. Figure 1c reveals a high-resolution TEM (HRTEM) image of a CuS_ySe_{1-y} nanoplate and its fast Fourier transform (FFT) that shows a 6-fold symmetry. The enlarged details of the nanoplate in the frame of Figure 1c are presented in Figure 1d. The lattice fringe with a spacing of 0.33 nm matches well with the spacing between the {100} planes of the hexagonal alloy in Figure 1a. The EDS result in Supporting Information, Figure S1a,

16353

dx.doi.org/10.1021/am5046247 | ACS Appl. Mater. Interfaces 2014, 6, 16352–16359

indicates the nanoplates have an atomic ratio of Cu:S:Se = 50:27:23, i.e., $CuS_{0.54}Se_{0.46}$ ($y = 0.54$).

Figure 2a shows the XRD pattern of the product upon annealing the above-mentioned precursor solution at 100 °C

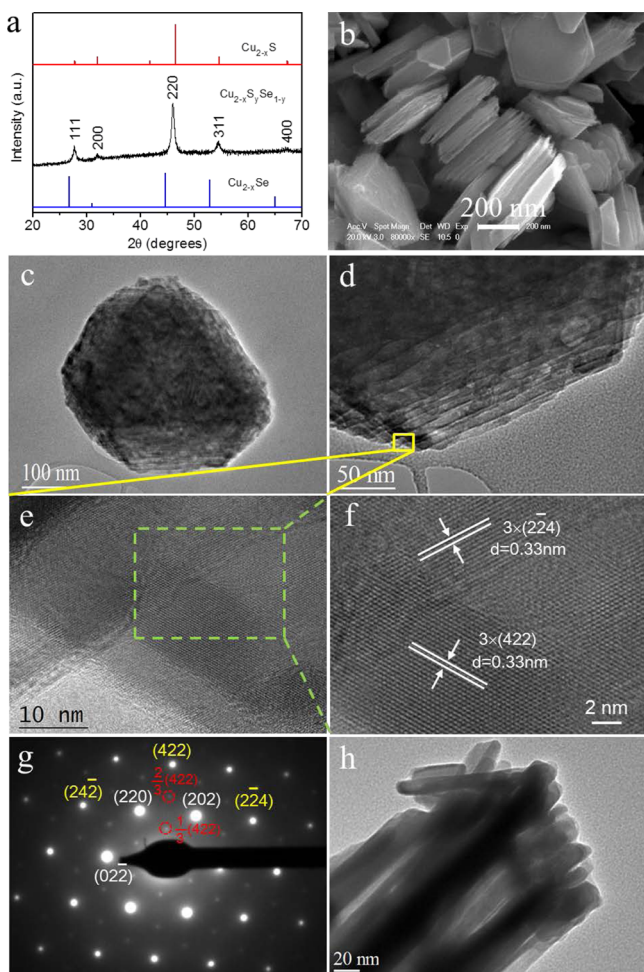**Figure 2.** (a) XRD pattern, (b) SEM image, (c, d) TEM images, (e, f) HRTEM images, and (g) SAED pattern of the fcc $Cu_{2-x}S_ySe_{1-y}$ ($x = 0.37$, $y = 0.63$) single-crystal-like stacked nanoplate assemblies prepared with 0.75 mmol of S and 1.25 mmol of Se in the reactants. (h) TEM image of a nanoplate stack with edge-on orientation.

for 10 h. It is interesting that the product transformed to have an fcc structure. Diffraction peaks of the products are between those of the fcc $Cu_{2-x}Se$ (JCPDF 06-0680) and the fcc $Cu_{2-x}S$ (JCPDF 02-1292) binary phases. An SEM image of the product (Figure 2b) reveals that the fcc alloy consists of stacks of nanoplates with thicknesses of 50−100 nm and a lateral dimension of 400−600 nm. The compactly stacked nanoplates are further demonstrated by TEM images as shown in Figure 2c,d. HRTEM images in Figure 2e,f show that the stacked nanoplates have lattice spacings of 0.33 nm which can be indexed to the 3 × {422} planes of an fcc structure.[13,22,30−32] Figure 2g shows a selected area electron diffraction (SAED) pattern along the $[\bar{1}11]$ zone axis of the stacked nanoplates in Figure 2c. All diffraction spots are of the same set of crystallographic patterns, indicating that all the nanoplates in the stack have the same orientation and that the whole stack is a single-crystal-like assembly. Figure 2h shows a TEM image of a nanoplate stack with an edge-on orientation. The thickness of

an individual nanoplate is estimated to be about 10 nm. Parts b, c, and d, of Figure S2 in the Supporting Information are, respectively, Cu, S, and Se elemental EDS mappings of the stacked nanoplate assembly in Supporting Information, Figure S2a, revealing homogeneous distributions of the three elements throughout the nanoplate assembly. The EDS spectrum in Figure S1b in the Supporting Information shows that the Cu:S:Se atomic ratio of the single-crystal-like assemblies is 62:24:14, i.e., $Cu_{1.63}S_{0.63}Se_{0.37}$ ($x = 0.37$, $y = 0.63$).

The evolution process from isolated hexagonal nanoplates to cubic single-crystal-like stacked nanoplate assemblies was observed by taking samples upon annealing for different durations. Figure 3a shows that nanoplates have a lateral dimension of 100−200 nm before annealing. After 2 h of annealing, the CuS_ySe_{1-y} nanoplates in the solution have grown into larger sizes of 200−400 nm. After 6 h of annealing, aggregation and oriented stacking of CuS_ySe_{1-y} nanoplates along the [001] direction are observed as shown in Figure 3c. The XRD pattern in Figure 4 reveals that the CuS_ySe_{1-y} phase at this stage is still hexagonal with a Cu:S:Se atomic ratio of 53:26:21 (Supporting Information, Table S1), showing a slightly copper rich content. When annealing is further prolonged to 7.5 h, the assemblies of well-stacked nanoplates are formed. XRD data in Figure 4c reveal that the sample consists of both hexagonal and fcc phases, indicating that chemical reaction and phase conversion from hexagonal CuS_ySe_{1-y} to fcc $Cu_{2-x}S_ySe_{1-y}$ mainly occur at this stage. After 8.5 h of annealing, pure fcc phase $Cu_{2-x}S_ySe_{1-y}$ single-crystal-like stacked nanoplate assemblies are formed. Similar phase conversion from hexagonal to fcc structure in binary copper selenides has also been reported.[13,33] The single-crystal-like assemblies with a Cu:S:Se atomic ratio of 62:24:14 (i.e., $x = 0.37$, $y = 0.63$) are obtained after 10 h of annealing at 100 °C. The formation of such single-crystal-like assemblies is considered to be the combined effects of oriented stacking coupled with Ostwald-ripening upon annealing.[34−37] Composition changes from the hexagonal CuS_ySe_{1-y} before annealing to the fcc $Cu_{2-x}S_ySe_{1-y}$ after 10 h of annealing are revealed to show obvious increases of both copper content and S/Se ratio. While S content shows a slight decrease from 27% for hexagonal CuS_ySe_{1-y} to 24% for fcc $Cu_{2-x}S_ySe_{1-y}$, Se content is dramatically decreasing from 23 to 14% (Supporting Information, Table S1), indicating that Se ions diffuse much faster from the nanoplates into solution during the phase conversion process.

Figure 5 shows Raman spectra of the samples obtained with different annealing durations. Three peaks are observed in each spectrum of the ternary Cu−S−Se samples, including a peak of the Se−Se stretching mode (268−270 cm^{-1}), a peak of the S−S stretching mode (448−453 cm^{-1}), and a peak of the S−Se stretching mode (370−373 cm^{-1}).[38] The resonance peak of the S−Se stretching vibration can be viewed as a characteristic peak of the ternary Cu−S−Se alloy. Compared with the hexagonal CuS_ySe_{1-y} nanoplates before annealing, the fcc $Cu_{2-x}S_ySe_{1-y}$ stacked nanoplate assemblies obtained after 10 h of annealing show obviously decreased Se−Se band intensity, also suggesting less Se content. The peaks of S−S, S−Se, and Se−Se stretching modes shift to higher wavenumbers from hexagonal CuS_ySe_{1-y} to fcc $Cu_{2-x}S_ySe_{1-y}$ due to the increasing S/Se atomic ratio of the fcc $Cu_{2-x}S_ySe_{1-y}$ upon annealing.

Figure 6 shows UV−vis absorption spectra of the ternary Cu−S−Se samples obtained by annealing the precursor solution with different durations. All samples show similar
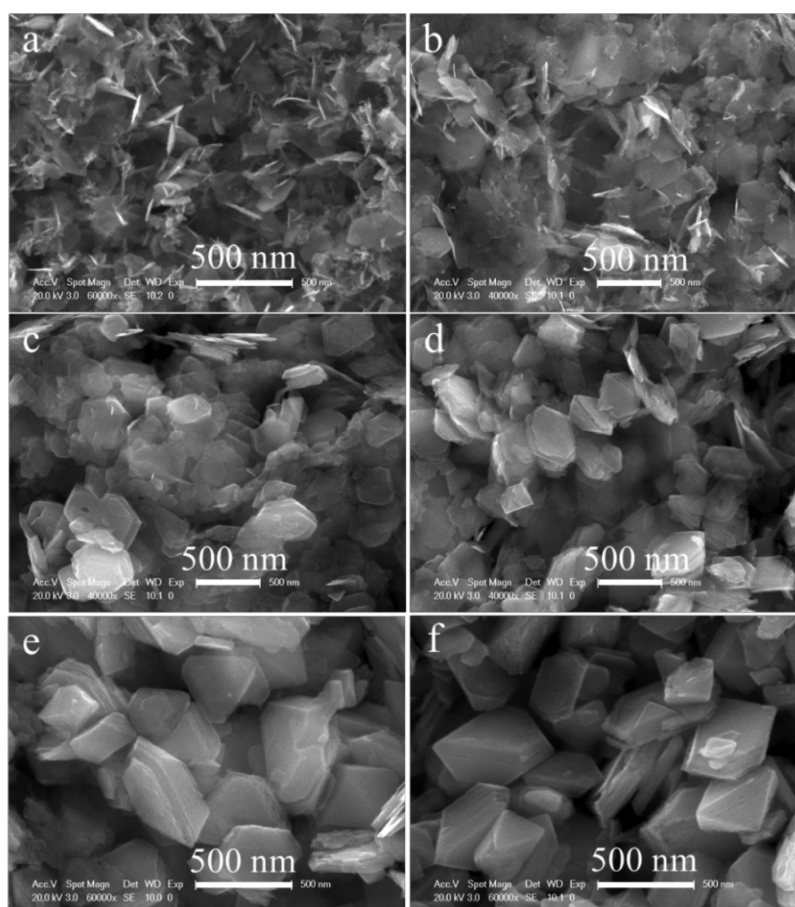
Figure 3. SEM images samples obtained with different annealing durations, showing the evolution process from CuS_ySe_{1-y} nanoplates to $Cu_{2-x}S_ySe_{1-y}$ single-crystal-like stacked nanoplate assemblies: (a) 0, (b) 2, (c) 6, (d) 7.5, (e) 8.5, and (f) 10 h.
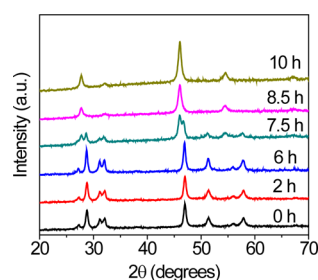

Figure 4. XRD patterns of Cu−S−Se samples obtained with different annealing durations, showing the phase conversion from hexagonal to fcc phase.

Figure 6. UV−vis spectra of samples prepared with various annealing durations, revealing red-shift absorption from hexagonal to cubic phase: (a) 0, (b) 2, (c) 6, (d) 7.5, (e) 8.5, and (f) 10 h.
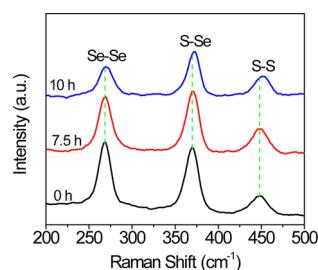

Figure 5. Raman spectra of samples obtained with different annealing durations: (a) 0, (b) 7.5, and (c) 10 h.

absorbance shapes with a direct band-gap absorption in the visible region and a broad absorption in the near-infrared
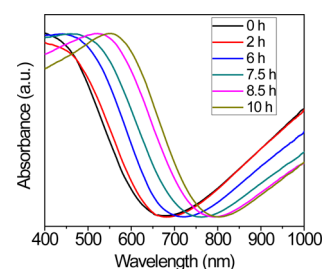
(NIR) region due to the localized surface plasmon resonance (LSPR) of free holes in the valence band.[15−19] The hexagonal CuS_ySe_{1-y} nanoplates before annealing show an absorption edge at 614 nm (2.02 eV). A significant red shift is observed for samples upon annealing. The absorption edge is continuously shifted to 629 nm (1.97 eV) for the CuS_ySe_{1-y} nanoplates with 2 h of annealing, to 656 nm (1.89 eV) for the CuS_ySe_{1-y} nanoplates with 6 h of annealing, to 693 nm (1.79 eV) for the mixed hexagonal CuS_ySe_{1-y} and fcc $Cu_{2-x}S_ySe_{1-y}$ obtained after 7.5 h of annealing, and further to 743 nm (1.67 eV) for the fcc $Cu_{2-x}S_ySe_{1-y}$ prepared after 10 h of annealing. Slightly smaller slopes of NIR absorption (Figure 6) as the Cu−S−Se alloys evolve from hexagonal to fcc structure are observed probably due to the decreased copper vacancies, which is similar to the case in binary copper chalcogenides.[15−19]

Furthermore, it was found that composition of the fcc $Cu_{2-x}S_ySe_{1-y}$ single-crystal-like stacked nanoplate assemblies can be easily tuned by adjusting the ratio of sulfur/selenium in the reactants. Panels i−iv in Figure 7a show respectively SEM
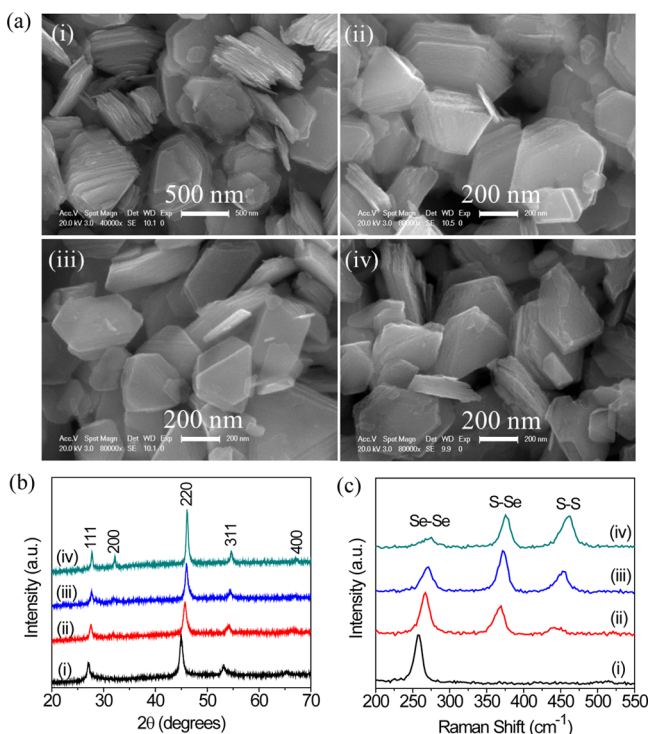

Figure 7. (a) SEM images, (b) XRD patterns, and (c) Raman spectra of $Cu_{2-x}S_ySe_{1-y}$ single-crystal-like stacked nanoplate assemblies with different S contents (y). (i) $y = 0$, (ii) $y = 0.42$, (iii) $y = 0.63$, and (iv) $y = 0.76$.

images of Cu−S−Se products prepared with S:Se molar ratios of (i) 0:2, (ii) 0.5:1.5, (iii) 0.75:1.25, and (iv) 1:1. All samples show similar morphologies of stacked nanoplate assemblies. Their corresponding XRD patterns are presented in Figure 7b. Curve i shows an XRD pattern of the product prepared without S in the reactants; all the diffraction peaks match well with the fcc $Cu_{2-x}Se$ phase (JCPDF 06-0680). A continuous shift of the diffraction peaks toward higher 2θ degrees with increasing S content (y) is observed, indicating the formation of the alloyed fcc phase of $Cu_{2-x}S_ySe_{1-y}$ with differing S content (y). Figure 7c shows corresponding Raman spectra of the fcc $Cu_{2-x}S_ySe_{1-y}$ stacked nanoplate assemblies with varying S content (y). Spectrum i of $Cu_{2-x}Se$ in Figure 7c shows a resonance peak located at 260 cm^{-1} attributed to the Se−Se stretching vibration mode, which is in good agreement with the previous report.[39] Spectra ii−iv show the Raman spectra of ternary $Cu_{2-x}S_ySe_{1-y}$ with increasing S content (y). All exhibit three resonance peaks corresponding respectively to the Se−Se, the S−Se, and the S−S vibration modes, which shift to higher wavenumbers with increasing S content (y). This result also demonstrates the formation of alloyed $Cu_{2-x}S_ySe_{1-y}$ stacked nanoplate assemblies with a tunable chalcogen composition.

Quantum dot sensitized solar cells (QDSSCs) are promising photovoltaic devices with the advantages of high theoretical power conversion efficiency (44%), low temperature synthesis, low production cost, and easy device fabrication.[40−48] The photovoltaic performance of QDSSCs is not only determined by the photoanodes, but also dramatically affected by the

counter electrodes (CEs). CEs in QDSSCs play key roles in receiving and injecting electrons from the external circuit to the polysulfide electrolyte (S^{2-}/S_n^{2-}) and electrocatalyzing redox couple regeneration by reducing the oxidized state (S_n^{2-}) into its reduced state (S^{2-}).[42,43] Exploration of low-cost, earth abundant, and environmentally friendly CEs with high electrocatalytic activities to replace the traditional noble metal Pt electrode is of great significance.[49−56] In this work, the Cu−S−Se alloys are employed for the first time as new and highly efficient CE materials in QDSSCs. The hexagonal CuS_ySe_{1-y} ($y = 0.54$) nanoplates before annealing and the fcc $Cu_{2-x}S_ySe_{1-y}$ ($x = 0.37$, $y = 0.63$) stacked nanoplate assemblies after 10 h of annealing, which were deposited on FTO glass substrates with thicknesses of about 3.8 μm (as shown in Supporting Information, Figure S3), are studied to investigate their electrocatalytic activities for polysulfide electrolyte regeneration in QDSSCs. Figure 8 shows Nyquist plots of Pt/FTO,
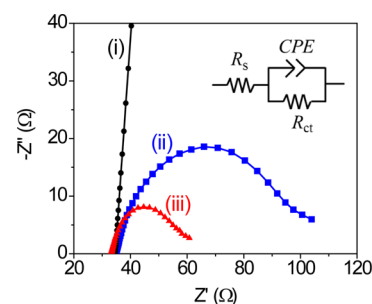

Figure 8. Nyquist plots of various symmetric dummy cells containing polysulfide redox electrolyte. (i) Pt/FTO, (ii) $Cu_{2-x}S_ySe_{1-y}$/FTO ($x = 0.37$, $y = 0.63$), and (iii) CuS_ySe_{1-y}/FTO ($y = 0.54$). The active area of the cells is 0.25 cm^2. The inset circuit diagram shows the equivalent circuit used to fit the plots and extract the charge transfer resistance. R_s, series resistance; R_{ct}, charge transfer resistance at the CE/electrolyte interface; CPE, constant phase element of electrical double layer at the CE/electrolyte interface.

CuS_ySe_{1-y}/FTO, and $Cu_{2-x}S_ySe_{1-y}$/FTO symmetric cells containing polysulfide electrolyte measured in the frequency range 0.1−10^5 Hz under dark conditions. The full Nyquist plot of the Pt/FTO symmetric cell is presented in the Supporting Information, Figure S4. A simplified Randles equivalent circuit, as shown in the inset of Figure 8, is employed to fit the Nyquist plots. All three plots show a single semicircle corresponding to the charge transfer resistance (R_{ct}) at the CE/electrolyte interface, and the diffusion impedance of redox species in the electrolyte is not observed. This observation is in agreement with previous reports,[49−54] and was explained by some research groups that when the R_{ct} at higher frequencies is dramatically larger than the diffusion impedance at lower frequencies, the semicircle of R_{ct} would hide the appearance of the ion diffusion behavior.[51,57] It is clear that the value of R_{ct} decreases significantly from 9.6×10^3 Ω for the Pt/FTO to 72 Ω for the $Cu_{2-x}S_ySe_{1-y}$/FTO, and further to 28 Ω for the CuS_ySe_{1-y}/FTO, although the three electrodes exhibit a similar series resistance (R_s) of ∼34 Ω. The R_{ct} has been viewed as an indicator for the electrocatalytic activity of the electrode. The EIS data indicate that the CuS_ySe_{1-y} nanoplates and the $Cu_{2-x}S_ySe_{1-y}$ assemblies are more efficient CE materials than noble metal Pt for polysulfide electrolyte regeneration in QDSSCs. Furthermore, as compared to the fcc $Cu_{2-x}S_ySe_{1-y}$ stacked nanoplate assemblies, the smaller R_{ct} of the CuS_ySe_{1-y}/FTO indicates that the hexagonal CuS_ySe_{1-y} nanoplates show

higher capability for transferring electrons from the CE to the polysulfide electrolyte, probably due to the smaller size and nonaggregation that would provide more edges for better electrocatalytic properties.

QDSSCs using hexagonal CuS_ySe_{1-y} nanoplates, fcc $Cu_{2-x}S_ySe_{1-y}$ stacked nanoplate assemblies, and Pt as CEs were fabricated by assembling with a photoanode of a ZnO/ZnSe/CdSe/ZnSe nanocable array (Supporting Information, Figure S5) to evaluate their photovoltaic performance. Figure 9
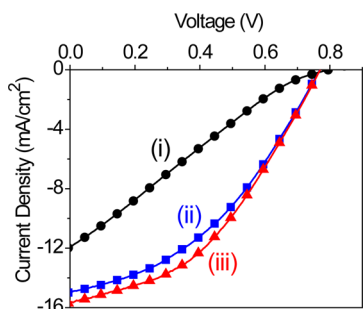

Figure 9. Current density–voltage (J–V) characteristics of the QDSSCs using various counter electrodes: (i) Pt/FTO, (ii) $Cu_{2-x}S_ySe_{1-y}$/FTO (x = 0.37, y = 0.63), and (iii) CuS_ySe_{1-y}/FTO (y = 0.54).

shows the current density–voltage (J–V) characteristics of the various QDSSCs, and the performance parameters are summarized in Table 1. The device using a Pt/FTO CE

Table 1. Photovoltaic Parameters Obtained from the J–V Curves Using Various CEs[a]

CE	J_{SC} (mA/cm^2)	V_{OC} (V)	FF	PCE (%)
CuS_ySe_{1-y} (y = 0.54)	15.69	0.772	0.419	5.01
$Cu_{2-x}S_ySe_{1-y}$ (x = 0.37, y = 0.63)	14.96	0.768	0.396	4.63
Pt	11.92	0.797	0.223	2.13

[a]J_{SC}, short circuit current density; V_{OC}, open circuit voltage; FF, fill factor; PCE, power conversion efficiency.

shows a J_{SC} of 11.92 mA cm^{-2}, a V_{OC} of 0.797 V, and an FF of 0.223, and presents a power conversion efficiency (PCE) of 2.13%. Significant enhancement of the photovoltaic performance is observed by replacing the Pt/FTO CE with CuS_ySe_{1-y} and $Cu_{2-x}S_ySe_{1-y}$ CE materials. The cell using the $Cu_{2-x}S_ySe_{1-y}$/FTO (x = 0.37, y = 0.63) CE yields a PCE of 4.63% with an increased FF of 0.396 V and J_{SC} of 14.96 mA cm^{-2}. When the CuS_ySe_{1-y}/FTO (y = 0.54) CE is employed, FF and J_{SC} of the cell using the same photoanode are further improved to 0.419 and 15.69 mA cm^{-2}, respectively, resulting in an increased PCE as high as 5.01%. In our case, more than five photoanode samples were measured with various CEs. All results show good repeatability that both the hexagonal and the fcc Cu–S–Se samples act as more active CE materials than noble Pt; in particular, the hexagonal CuS_ySe_{1-y} based solar cells show even better photovoltaic performance as compared to those of the fcc $Cu_{2-x}S_ySe_{1-y}$ based device.

CONCLUSIONS

In summary, homogeneously alloyed ternary hexagonal CuS_ySe_{1-y} nanoplates and fcc $Cu_{2-x}S_ySe_{1-y}$ single-crystal-like stacked nanoplate assemblies with tunable S/Se ratios have

been controllably synthesized via a simple and low-temperature solution method. Phase conversion of ternary hexagonal CuS_ySe_{1-y} nanoplates to fcc $Cu_{2-x}S_ySe_{1-y}$ stacked nanoplate assemblies is investigated, in which hexagonal CuS_ySe_{1-y} nanoplates are assembled and oriented along the [001] direction to form stacked nanoplate assemblies. During the phase conversion process, both S and Se ions diffuse out from the nanoplates; particularly Se ions diffuse much faster than S ions, resulting in an increase of the S/Se ratio. A continuous red shift of band-gap absorption is revealed during the phase evolution from hexagonal CuS_ySe_{1-y} to fcc $Cu_{2-x}S_ySe_{1-y}$. Both hexagonal and fcc ternary Cu–S–Se semiconductors show Raman resonance peaks of S–S, S–Se, and Se–Se vibration modes, which shift to high wavenumbers with increasing S/Se ratio. The hexagonal CuS_ySe_{1-y} nanoplates and fcc $Cu_{2-x}S_ySe_{1-y}$ stacked nanoplate assemblies have been demonstrated as low-cost and highly efficient CE materials for polysulfide electrolyte regeneration in QDSSCs. The cells using $Cu_{2-x}S_ySe_{1-y}$/FTO (x = 0.37, y = 0.63) CE and CuS_ySe_{1-y}/FTO (y = 0.54) CE yield PCEs of 4.63 and 5.01%, respectively, while the cell using noble Pt/FTO CE shows a PCE of 2.13%.

ASSOCIATED CONTENT

Ⓢ Supporting Information

Table of Cu:S:Se atomic ratio of Cu–S–Se samples (0.75 mmol of S and 1.25 mmol of Se in the reactants) obtained with different annealing durations; EDS spectra of hexagonal CuS_ySe_{1-y} nanoplates and fcc $Cu_{2-x}S_ySe_{1-y}$ stacked nanoplate assemblies; STEM image of fcc $Cu_{2-x}S_ySe_{1-y}$ stacked nanoplate assemblies and corresponding EDS mappings of Cu, S, and Se elements; cross-section SEM images of CuS_ySe_{1-y}/FTO (y = 0.54) CE and $Cu_{2-x}S_ySe_{1-y}$/FTO (x = 0.37, y = 0.63) CE; Nyquist plot of Pt/FTO symmetric dummy cell containing polysulfide redox electrolyte; SEM image of ZnO/ZnSe/CdSe/ZnSe nanocable array. This material is available free of charge via the Internet at http://pubs.acs.org.

AUTHOR INFORMATION

Corresponding Authors
*E-mail: apjunxu@hfut.edu.cn.
*E-mail: apcslee@cityu.edu.hk.

Notes
The authors declare no competing financial interest.

REFERENCES

(1) Swafford, L. A.; Weigand, L. A.; Bowers, M. J., II; McBride, J. R.; Rapaport, J. L.; Watt, T. L.; Dixit, S. K.; Feldman, L. C.; Rosenthal, S. J. Homogeneously Alloyed CdS$_x$Se$_{1-x}$ Nanocrystals: Synthesis, Characterization, and Composition/Size-Dependent Band Gap. *J. Am. Chem. Soc.* **2006**, *128*, 12299–12306.

(2) Wang, M.; Fei, G. T.; Zhang, Y. G.; Kong, M. G.; Zhang, L. D. Tunable and Predetermined Bandgap Emissions in Alloyed ZnS$_x$Se$_{1-x}$ Nanowires. *Adv. Mater.* **2007**, *19*, 4491–4494.

(3) Xu, H.; Liang, Y.; Liu, Z.; Zhang, X.; Hark, S. Synthesis and Optical Properties of Tetrapod-Like ZnSSe Alloy Nanostructures. *Adv. Mater.* **2008**, *20*, 3294–3297.

16357

dx.doi.org/10.1021/am5046247 | ACS Appl. Mater. Interfaces 2014, 6, 16352−16359

(4) Pan, A.; Yang, H.; Liu, R.; Yu, R.; Zou, B.; Wang, Z. Color-Tunable Photoluminescence of Alloyed CdS$_x$Se$_{1-x}$ Nanobelts. *J. Am. Chem. Soc.* **2005**, *127*, 15692−15693.

(5) Xu, J.; Yang, X.; Wang, H.; Chen, X.; Luan, C.; Xu, Z.; Lu, Z.; Roy, V. A. L.; Zhang, W.; Lee, C.-S. Arrays of ZnO/Zn$_x$Cd$_{1-x}$Se Nanocables: Band Gap Engineering and Photovoltaic Applications. *Nano Lett.* **2011**, *11*, 4138−4143.

(6) Zhong, X.; Feng, Y.; Knoll, W.; Han, M. Alloyed Zn$_x$Cd$_{1-x}$S Nanocrystals with Highly Narrow Luminescence Spectral Width. *J. Am. Chem. Soc.* **2003**, *125*, 13559−13563.

(7) Zhao, Y.; Burda, C. Development of Plasmonic Semiconductor Nanomaterials with Copper Chalcogenides for a Future with Sustainable Energy Materials. *Energy Environ. Sci.* **2012**, *5*, 5564−5576.

(8) Xu, J.; Lee, C.-S.; Tang, Y.-B.; Chen, X.; Chen, Z.-H.; Zhang, W.-J.; Lee, S.-T.; Zhang, W.; Yang, Z. Large-Scale Synthesis and Phase Transformation of CuSe, CuInSe$_2$, and CuInSe$_2$/CuInS$_2$ Core/Shell Nanowire Bundles. *ACS Nano* **2010**, *4*, 1845−1850.

(9) Fan, F.-J.; Wu, L.; Yu, S.-H. Energetic I−III−VI$_2$ and I$_2$−II−IV−VI$_4$ Nanocrystals: Synthesis, Photovoltaic and Thermoelectric Applications. *Energy Environ. Sci.* **2014**, *7*, 190−208.

(10) Wu, Y.; Wadia, C.; Ma, W.; Sadtler, B.; Alivisatos, A. P. Synthesis and Photovoltaic Application of Copper(I) Sulfide Nanocrystals. *Nano Lett.* **2008**, *8*, 2551−2555.

(11) Tian, Q.; Tang, M.; Sun, Y.; Zou, R.; Chen, Z.; Zhu, M.; Yang, S.; Wang, J.; Wang, J.; Hu, J. Hydrophilic Flower-Like CuS Superstructures as an Efficient 980 nm Laser-Driven Photothermal Agent for Ablation of Cancer Cells. *Adv. Mater.* **2011**, *23*, 3542−3547.

(12) Du, Y.; Yin, Z.; Zhu, J.; Huang, X.; Wu, X.-J.; Zeng, Z.; Yan, Q.; Zhang, H. A General Method for the Large-Scale Synthesis of Uniform Ultrathin Metal Sulphide Nanocrystals. *Nat. Commun.* **2012**, *3*, 1177.

(13) Xu, J.; Zhang, W.; Yang, Z.; Ding, S.; Zeng, C.; Chen, L.; Wang, Q.; Yang, S. Large-Scale Synthesis of Long Crystalline Cu$_{2-x}$Se Nanowire Bundles by Water-Evaporation-Induced Self-Assembly and Their Application in Gas Sensing. *Adv. Funct. Mater.* **2009**, *19*, 1759−1766.

(14) Wu, C.-Y.; Wu, Y.-L.; Wang, W.-J.; Mao, D.; Yu, Y.-Q.; Wang, L.; Xu, J.; Hu, J.-G.; Luo, L.-B. High Performance Nonvolatile Memory Devices Based on Cu$_{2-x}$Se Nanowires. *Appl. Phys. Lett.* **2013**, *103*, 193501.

(15) Luther, J. M.; Jain, P. K.; Ewers, T.; Alivisatos, A. P. Localized Surface Plasmon Resonances Arising from Free Carriers in Doped Quantum Dots. *Nat. Mater.* **2011**, *10*, 361−366.

(16) Zhao, Y.; Pan, H.; Lou, Y.; Qiu, X.; Zhu, J.; Burda, C. Plasmonic Cu$_{2−x}$S Nanocrystals: Optical and Structural Properties of Copper-Deficient Copper(I) Sulfides. *J. Am. Chem. Soc.* **2009**, *131*, 4253−4261.

(17) Xie, Y.; Riedinger, A.; Prato, M.; Casu, A.; Genovese, A.; Guardia, P.; Sottini, S.; Sangregorio, C.; Miszta, K.; Ghosh, S.; Pellegrino, T.; Manna, L. Copper Sulfide Nanocrystals with Tunable Composition by Reduction of Covellite Nanocrystals with Cu$^+$ Ions. *J. Am. Chem. Soc.* **2013**, *135*, 17630−17637.

(18) Liu, X.; Wang, X.; Zhou, B.; Law, W.-C.; Cartwright, A. N.; Swihart, M. T. Size-Controlled Synthesis of Cu$_{2-x}$E (E = S, Se) Nanocrystals with Strong Tunable Near-Infrared Localized Surface Plasmon Resonance and High Conductivity in Thin Films. *Adv. Funct. Mater.* **2013**, *23*, 1256−1264.

(19) Dorfs, D.; Härtling, T.; Miszta, K.; Bigall, N. C.; Kim, M. R.; Genovese, A.; Falqui, A.; Povia, M.; Manna, L. Reversible Tunability of the Near-Infrared Valence Band Plasmon Resonance in Cu$_{2-x}$Se Nanocrystals. *J. Am. Chem. Soc.* **2011**, *133*, 11175−11180.

(20) Guo, Q.; Ford, G. M.; Hillhouse, H. W.; Agrawal, R. Sulfide Nanocrystal Inks for Dense Cu(In$_{1-x}$Ga$_x$)(S$_{1-y}$Se$_y$)$_2$ Absorber Films and Their Photovoltaic Performance. *Nano Lett.* **2009**, *9*, 3060−3065.

(21) Riha, S. C.; Parkinson, B. A.; Prieto, A. L. Compositionally Tunable Cu$_2$ZnSn(S$_{1-x}$Se$_x$)$_4$ Nanocrystals: Probing the Effect of Se-Inclusion in Mixed Chalcogenide Thin Films. *J. Am. Chem. Soc.* **2011**, *133*, 15272−15275.

(22) Xu, J.; Tang, Y.-B.; Chen, X.; Luan, C.-Y.; Zhang, W.-F.; Zapien, J. A.; Zhang, W.-J.; Kwong, H.-L.; Meng, X.-M.; Lee, S.-T.; Lee, C.-S. Synthesis of Homogeneously Alloyed Cu$_{2-x}$(S$_y$Se$_{1-y}$) Nanowire Bundles with Tunable Compositions and Bandgaps. *Adv. Funct. Mater.* **2010**, *20*, 4190−4195.

(23) Wang, J.-J.; Xue, D.-J.; Guo, Y.-G.; Hu, J.-S.; Wan, L.-J. Bandgap Engineering of Monodispersed Cu$_{2-x}$S$_y$Se$_{1-y}$ Nanocrystals through Chalcogen Ratio and Crystal Structure. *J. Am. Chem. Soc.* **2011**, *133*, 18558−18561.

(24) Saldanha, P. L.; Brescia, R.; Prato, M.; Li, H.; Povia, M.; Manna, L.; Lesnyak, V. Generalized One-Pot Synthesis of Copper Sulfide, Selenide-Sulfide, and Telluride-Sulfide Nanoparticles. *Chem. Mater.* **2014**, *26*, 1442−1449.

(25) Liu, X.; Wang, X.; Swihart, M. T. Cu$_{2−x}$S$_{1−y}$Se$_y$ Alloy Nanocrystals with Broadly Tunable Near-Infrared Localized Surface Plasmon Resonance. *Chem. Mater.* **2013**, *25*, 4402−4408.

(26) Han, S.-K.; Gong, M.; Wang, Z.-M.; Gu, C.; Yu, S.-H. Colloidal Synthesis of Cu$_2$S$_x$Se$_{1−x}$ Hexagonal Nanoplates and Their Transformation to CdS$_x$Se$_{1−x}$ and ZnS$_x$Se$_{1−x}$ by the Cation-Exchange Reaction. *Part. Part. Syst. Charact.* **2013**, *30*, 1024−1029.

(27) Dilena, E.; Dorfs, D.; George, C.; Miszta, K.; Povia, M.; Genovese, A.; Casu, A.; Prato, M.; Manna, L. Colloidal Cu$_{2-x}$(S$_y$Se$_{1-y}$) Alloy Nanocrystals with Controllable Crystal Phase: Synthesis, Plasmonic Properties, Cation Exchange and Electrochemical Lithiation. *J. Mater. Chem.* **2012**, *22*, 13023−13031.

(28) Yan, K.; Zhang, L.; Qiu, J.; Qiu, Y.; Zhu, Z.; Wang, J.; Yang, S. A Quasi-Quantum Well Sensitized Solar Cell with Accelerated Charge Separation and Collection. *J. Am. Chem. Soc.* **2013**, *135*, 9531−9539.

(29) Xu, J.; Yang, X.; Yang, Q.-D.; Wong, T.-L.; Lee, S.-T.; Zhang, W.-J.; Lee, C.-S. Arrays of CdSe Sensitized ZnO/ZnSe Nanocables for Efficient Solar Cells with High Open-Circuit Voltage. *J. Mater. Chem.* **2012**, *22*, 13374−13379.

(30) Jin, R.; Cao, Y. W.; Mirkin, C. A.; Kelly, K. L.; Schatz, G. C.; Zheng, J. G. Photoinduced Conversion of Silver Nanospheres to Nanoprisms. *Science* **2001**, *294*, 1901−1903.

(31) Carim, A. H.; Lew, K.-K.; Redwing, J. M. Bicrystalline Silicon Nanowires. *Adv. Mater.* **2001**, *13*, 1489−1491.

(32) Germain, V.; Li, J.; Ingert, D.; Wang, Z. L.; Pileni, M. P. Stacking Faults in Formation of Silver Nanodisks. *J. Phys. Chem. B* **2003**, *107*, 8717−8720.

(33) Wu, X.-J.; Huang, X.; Liu, J.; Li, H.; Yang, J.; Li, B.; Huang, W.; Zhang, H. Two-Dimensional CuSe Nanosheets with Microscale Lateral Size: Synthesis and Template-Assisted Phase Transformation. *Angew. Chem., Int. Ed.* **2014**, *53*, 5083−5087.

(34) Zheng, J.; Huang, F.; Yin, S.; Wang, Y.; Lin, Z.; Wu, X.; Zhao, Y. Correlation between the Photoluminescence and Oriented Attachment Growth Mechanism of CdS Quantum Dots. *J. Am. Chem. Soc.* **2010**, *132*, 9528−9530.

(35) Liu, B.; Yu, S.-H.; Li, L.; Zhang, Q.; Zhang, F.; Jiang, K. Morphology Control of Stolzite Microcrystals with High Hierarchy in Solution. *Angew. Chem.* **2004**, *116*, 4849−4854.

(36) Jia, B.; Gao, L. Growth of Well-Defined Cubic Hematite Single Crystals: Oriented Aggregation and Ostwald Ripening. *Cryst. Growth Des.* **2008**, *8*, 1372−1376.

(37) Chen, G.; Xu, C.; Song, X.; Xu, S.; Ding, Y.; Sun, S. Template-free Synthesis of Single-Crystalline-like CeO$_2$ Hollow Nanocubes. *Cryst. Growth Des.* **2008**, *8*, 4449−4453.

(38) Ishii, M.; Shibata, K.; Nozaki, H. Anion Distributions and Phase Transitions in CuS$_{1-x}$Se$_x$ (x = 0−1) Studied by Raman Spectroscopy. *J. Solid State Chem.* **1993**, *105*, 504−511.

(39) Filippo, E.; Manno, D.; Serra, A. Synthesis and Growth Mechanism of Dendritic Cu$_{2-x}$Se Microstructures. *J. Alloys Compd.* **2012**, *538*, 8−10.

(40) Mora-Seró, I.; Bisquert, J. Breakthroughs in the Development of Semiconductor-Sensitized Solar Cells. *J. Phys. Chem. Lett.* **2010**, *1*, 3046−3052.

(41) Jun, H. K.; Careem, M. A.; Arof, A. K. Quantum Dot-Sensitized Solar Cells—Perspective and Recent Developments: A Review of Cd Chalcogenide Quantum Dots as Sensitizers. *Renewable Sustainable Energy Rev.* **2013**, *22*, 148−167.

(42) Yang, Z.; Chen, C.-Y.; Roy, P.; Chang, H.-T. Quantum Dot-Sensitized Solar Cells Incorporating Nanomaterials. *Chem. Commun.* **2011**, *47*, 9561−9571.

(43) Xu, J.; Chen, Z.; Zapien, J. A.; Lee, C.-S.; Zhang, W. Surface Engineering of ZnO Nanostructures for Semiconductor-Sensitized Solar Cells. *Adv. Mater.* **2014**, *26*, 5337−5367.

(44) Selinsky, R. S.; Ding, Q.; Faber, M. S.; Wright, J. C.; Jin, S. Quantum Dot Nanoscale Heterostructures for Solar Energy Conversion. *Chem. Soc. Rev.* **2013**, *42*, 2963−2985.

(45) Pan, Z.; Mora-Seró, I.; Shen, Q.; Zhang, H.; Li, Y.; Zhao, K.; Wang, J.; Zhong, X.; Bisquert, J. High-Efficiency "Green" Quantum Dot Solar Cells. *J. Am. Chem. Soc.* **2014**, *136*, 9203−9210.

(46) Pan, Z.; Zhao, K.; Wang, J.; Zhang, H.; Feng, Y.; Zhong, X. Near Infrared Absorption of $CdSe_xTe_{1-x}$ Alloyed Quantum Dot Sensitized Solar Cells with More than 6% Efficiency and High Stability. *ACS Nano* **2013**, *7*, 5215−5222.

(47) Pan, Z.; Zhang, H.; Cheng, K.; Hou, Y.; Hua, J.; Zhong, X. Highly Efficient Inverted Type-I CdS/CdSe Core/Shell Structure QD-Sensitized Solar Cells. *ACS Nano* **2012**, *6*, 3982−3991.

(48) Zhu, Z.; Qiu, J.; Yan, K.; Yang, S. Building High-Efficiency CdS/CdSe-Sensitized Solar Cells with a Hierarchically Branched Double-Layer Architecture. *ACS Appl. Mater. Interfaces* **2013**, *5*, 4000−4005.

(49) Yang, Z.; Chen, C.-Y.; Liu, C.-W.; Li, C.-L.; Chang, H.-T. Quantum Dot-Sensitized Solar Cells Featuring CuS/CoS Electrodes Provide 4.1% Efficiency. *Adv. Energy Mater.* **2011**, *1*, 259.

(50) Faber, M. S.; Park, K.; Cabán-Acevedo, M.; Santra, P. K.; Jin, S. Earth-Abundant Cobalt Pyrite (CoS_2) Thin Film on Glass as a Robust, High-Performance Counter Electrode for Quantum Dot-Sensitized Solar Cells. *J. Phys. Chem. Lett.* **2013**, *4*, 1843−1849.

(51) Zhang, X.; Huang, X.; Yang, Y.; Wang, S.; Gong, Y.; Luo, Y.; Li, D.; Meng, Q. Investigation on New $CuInS_2$/Carbon Composite Counter Electrodes for CdS/CdSe Cosensitized Solar Cells. *ACS Appl. Mater. Interfaces* **2013**, *5*, 5954−5960.

(52) Xu, J.; Xiao, J.; Dong, J.; Luo, Y.; Li, D.; Meng, Q. A New in-situ Preparation Method to CuS Electrodes for CdS/CdSe Co-Sensitized Solar Cells. *Electrochim. Acta* **2014**, *127*, 180−185.

(53) Lin, C.-Y.; Teng, C.-Y.; Li, T.-L.; Lee, Y.-L.; Teng, H. Photoactive p-Type PbS as a Counter Electrode for Quantum Dot-Sensitized Solar Cells. *J. Mater. Chem. A* **2013**, *1*, 1155−1162.

(54) Xu, J.; Xue, H.; Yang, X.; Wei, H.; Li, W.; Li, Z.; Zhang, W.; Lee, C.-S. Synthesis of Honeycomb-like Mesoporous Pyrite FeS_2 Microspheres as Efficient Counter Electrode in Quantum Dots Sensitized Solar Cells. *Small* **2014**, DOI: 10.1002/smll.201401102.

(55) Yang, Y.; Zhu, L.; Sun, H.; Huang, X.; Luo, Y.; Li, D.; Meng, Q. Composite Counter Electrode Based on Nanoparticulate PbS and Carbon Black: Towards Quantum Dot-Sensitized Solar Cells with Both High Efficiency and Stability. *ACS Appl. Mater. Interfaces* **2012**, *4*, 6162−6168.

(56) Zhao, K.; Yu, H.; Zhang, H.; Zhong, X. Electroplating Cuprous Sulfide Counter Electrode for High-Efficiency Long-Term Stability Quantum Dot Sensitized Solar Cells. *J. Phys. Chem. C* **2014**, *118*, 5683−5690.

(57) González-Pedro, V.; Xu, X.; Mora-Seró, I.; Bisquert, J. Modeling High-Efficiency Quantum Dot Sensitized Solar Cells. *ACS Nano* **2010**, *4*, 5783−5790.